

# Microstructures and Mechanical Properties of Ti6Al4V Parts Fabricated by Selective Laser Melting and Electron Beam Melting

H.K. Rafi, N.V. Karthik, Haijun Gong, Thomas L. Starr, and Brent E. Stucker

(Submitted March 1, 2013; in revised form May 23, 2013; published online August 6, 2013)

This work compares two metal additive manufacturing processes, selective laser melting (SLM) and electron beam melting (EBM), based on microstructural and mechanical property evaluation of Ti6Al4V parts produced by these two processes. Tensile and fatigue bars conforming to ASTM standards were fabricated using Ti6Al4V ELI grade material. Microstructural evolution was studied using optical and scanning electron microscopy. Tensile and fatigue tests were carried out to understand mechanical properties and to correlate them with the corresponding microstructure. The results show differences in microstructural evolution between SLM and EBM processed Ti6Al4V and their influence on mechanical properties. The microstructure of SLM processed parts were composed of an  $\alpha'$  martensitic phase, whereas the EBM processed parts contain primarily  $\alpha$  and a small amount of  $\beta$  phase. Consequently, there are differences in tensile and fatigue properties between SLM- and EBM-produced Ti6Al4V parts. The differences are related to the cooling rates experienced as a consequence of the processing conditions associated with SLM and EBM processes.

**Keywords** EBM, fatigue testing, microstructure, SLM, tensile testing

## 1. Introduction

Selective laser melting (SLM) and electron beam melting (EBM) are two powder-bed fusion-based additive manufacturing processes used to fabricate metallic parts (Ref 1, 2). These processes are of interest due to several advantages over conventional manufacturing methods. Freedom to fabricate intricate geometries, optimum material usage, elimination of expensive tooling etc. are some of the notable advantages of additive manufacturing processes. In these processes the CAD model of the part is fed to the machine where pre-processing software slices the model into layers of finite thickness. A powder layer is deposited on to a base plate above the build platform. A focused laser/electron beam scans the powder-bed based on the sliced CAD data. The scanning results in localized melting and solidification of the powder to form a layer of the part. Subsequent layers are built one over the other by lowering the build platform equivalent to the layer thickness until the part is completed.

Selective laser melting utilizes a fiber laser heat source. The four main parameters in SLM are laser power, scan speed, hatch spacing, and layer thickness. Generally, the process is

characterized by high scanning speeds and high thermal gradients, leading to high cooling rates. High cooling rates result in non-equilibrium microstructures which may require heat treatment for certain applications. The SLM build chamber is continuously flushed with inert gas to reduce oxygen level. Typical layer thickness lies in the range of 20-100  $\mu\text{m}$ . SLM is capable of processing standard materials like Ti6Al4V, 316L, 17-4PH, 15-5PH, hot work steels, cobalt-based and nickel-based alloys (Ref 3) and more. A description of SLM processes has been detailed elsewhere (Ref 4).

Arcam EBM technology uses an electron beam to melt powder layer. Electron beam-powder interactions are substantially different than laser-powder interactions. The penetration depth of an electron beam into the irradiated material is multiple times greater than it is with a laser beam (Ref 5). When the high speed electron beam interacts with the powder layer, kinetic energy is converted into thermal energy, causing the powder to melt. The build chamber is kept at an elevated temperature (approx. 700 °C) in a vacuum environment. Elevated temperatures help minimize thermally induced residual stresses and the formation of non-equilibrium microstructures. The high intensity electron beam first preheats the powder at a very high scan speed, large focal spot, and low beam current. Preheating of the powder can help lower moisture content and thus reduce the possibility of oxygen pickup. More importantly preheating can reduce residual stress buildup by bringing down the temperature-gradient between successive layers during processing. The preheating stage is followed by a melting stage where the electron beam scans the powder at a lower scan speed, smaller spot size, and higher beam current. Once the build is completed the part is allowed to cool slowly from 700 °C to room temperature. Due to the higher beam intensities and scan available with electron beams, the EBM process is much faster than the SLM process. A description of EBM processes has been detailed elsewhere (Ref 6).

H.K. Rafi, N.V. Karthik, Haijun Gong, Thomas L. Starr, and Brent E. Stucker, Department of Industrial Engineering, JB Speed School of Engineering, University of Louisville, Louisville, KY 40292. Contact e-mails: khalidrafi@gmail.com and brent.stucker@louisville.edu.

Previous studies carried out by different researchers showed typical microstructures and related properties for SLM- and EBM-produced materials. Thijs et al. (Ref 7) studied the influence of process parameters and the scanning strategy on the microstructural evolution during SLM processing of Ti64. They observed the resulting microstructure as acicular martensite as a consequence of very high cooling rates. The microstructure was significantly affected by factors such as high localized heat inputs, very short interaction times, local heat transfer conditions, and processing conditions like scanning velocity, hatch spacing (the distance between two adjacent scan vectors), and scanning strategy. Facchini et al. also found SLM-produced Ti64 microstructures to be as completely martensitic. Song et al. (Ref 8) studied the effect of process parameters in terms of microstructure, densification, surface roughness, and microhardness for Ti64. They suggested a laser power of 110 W and scan speed of 0.4 m/s in a continuous melting mode to obtain a Ti64 part with maximum density. Other than the microstructural aspects, previous studies performed by Yadroitsev et al. (Ref 9), Morgan et al. (Ref 10), and Yasa et al. (Ref 11) have provided the details on the influence of substrate, energy input, laser pulsing, and laser irradiation parameters on process stability and dimensional accuracy of the final product.

Murr et al. (Ref 6) carried out characterization and comparison of Ti64 produced by EBM processing with wrought products. Microstructural characterization revealed acicular  $\alpha$  and associated  $\beta$  microstructure. Prior  $\beta$  grains form

epitaxially and extend through many layers which is a direct consequence of the thermal gradient in the build direction (Ref 12). Facchini et al. (Ref 13) also showed a very fine and acicular morphology when Ti64 parts were produced using EBM.

Although the microstructural aspects of SLM-produced and EBM-produced samples have been studied, little attention has been paid to a comparison and contrast between these processes with respect to a given material. Therefore, this work is aimed at comparing SLM and EBM processes in terms of microstructure, tensile properties, and fatigue properties of Ti64.

## 2. Experimental Methods

Ti64 parts were produced using an EOS M270 SLM machine and an Arcam S400 EBM machine. Ti64 powder was procured from each respective machine manufacturer. Powder particle size was measured using a “Microtare 3000” particle analyzer. The average particle size of the powder supplied by EOS was 36  $\mu\text{m}$  and the powder supplied by Arcam was 60  $\mu\text{m}$ . The particle size distribution and corresponding SEM-SE images of Arcam Ti64 powder and EOS Ti64 powder are shown in Fig. 1. Cylindrical specimens and specimens conforming to ASTM standards (ASTM: E8) for tensile testing and for fatigue testing (ASTM: E466) were fabricated. The as-built cylindrical specimens were analyzed for surface finish and

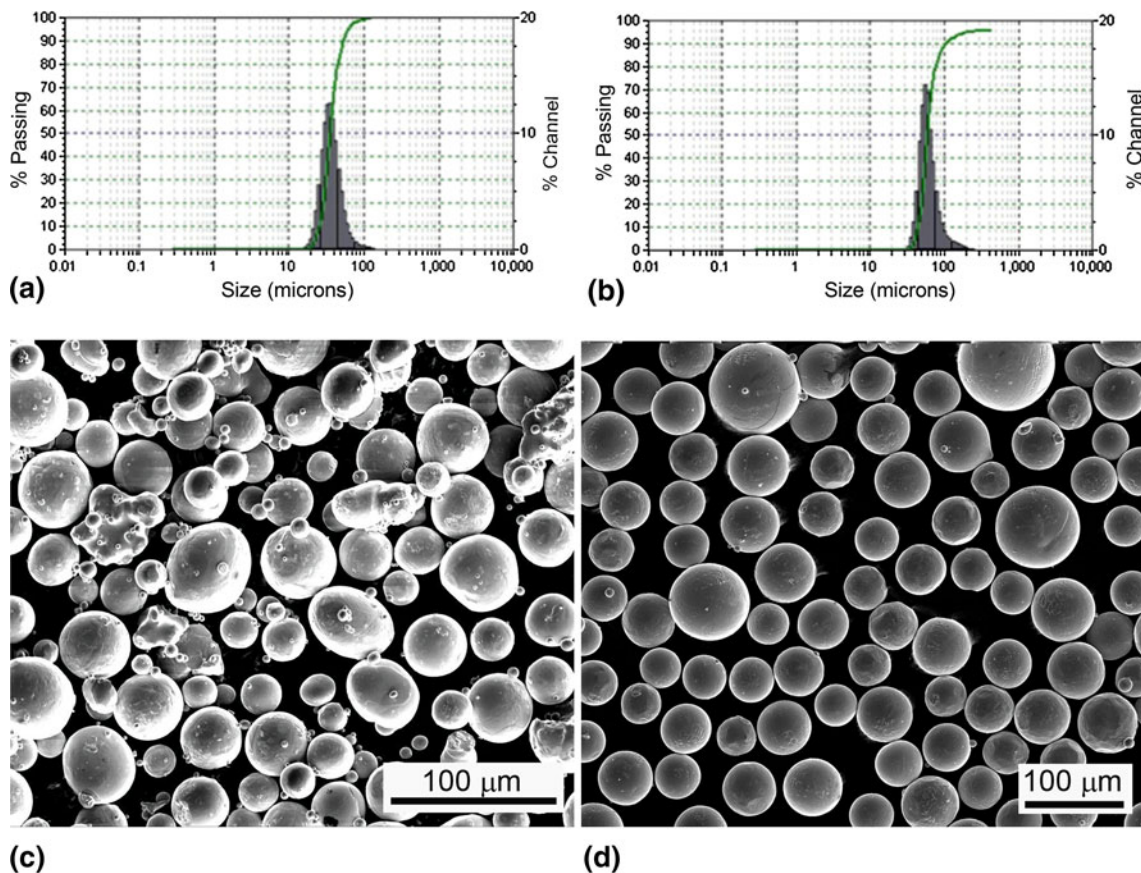


**Fig. 1** (a) Powder size distribution of EOS supplied Ti64 powder (avg. particle size: 36  $\mu\text{m}$ ). (b) Powder size distribution of Arcam supplied Ti64 powder (avg. particle size: 60  $\mu\text{m}$ ). (c) SEM-SE image of EOS supplied Ti64 powder. (d) SEM-SE image of Arcam supplied Ti64 powder

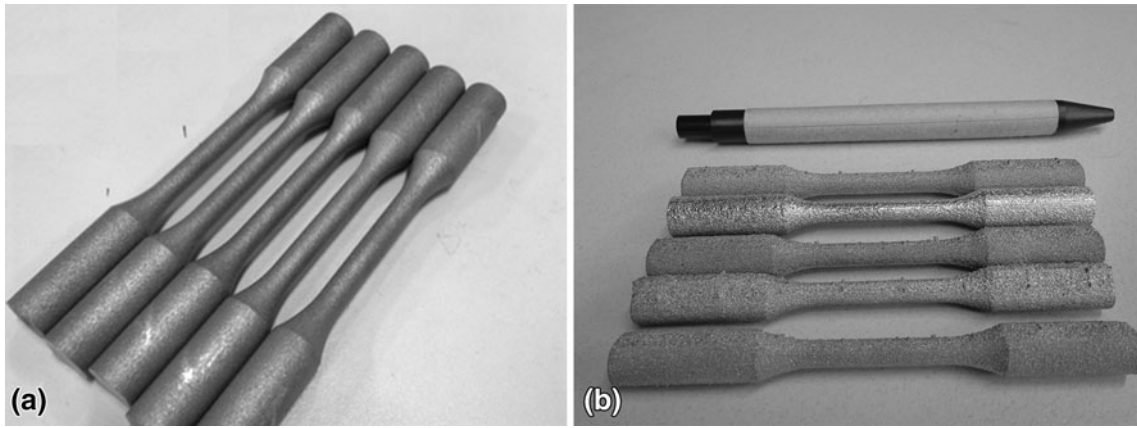


**Fig. 2** (a) As-built tensile samples produced in SLM. (b) As-built tensile samples produced in EBM

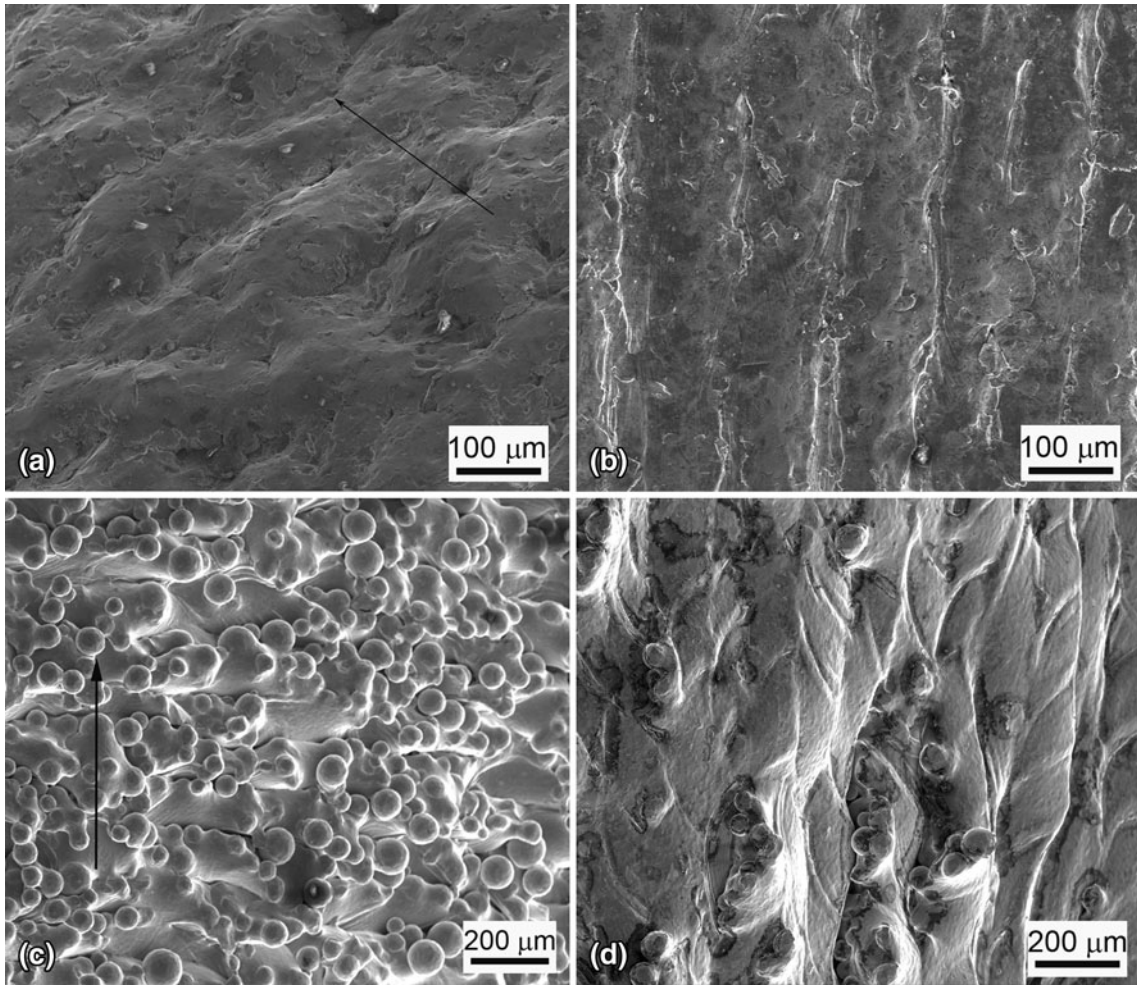


**Fig. 3** (a) External surface of a vertically built SLM sample (arrow shows the build direction). (b) External surface of a horizontally built SLM sample (build direction is perpendicular to the image plane). (c) External surface of a vertically built EBM sample (arrow shows the build direction). (d) External surface of a horizontally built EBM sample (build direction is perpendicular to the image plane)

sectioned for metallographic characterization. Metallographic specimens were prepared following standard specimen preparation methods. Optical microscopy (OM) and scanning electron microscopy (SEM) were used for microstructural characterization. SEM-EDS (energy dispersive spectroscopy)

was carried out to compare any compositional differences which may have occurred due to differences in processes characteristics. OM was carried out on an Olympus optical microscope and SEM was carried out in FEI FEG-SEM. X-ray diffraction (XRD) was carried out to analyze the differences in

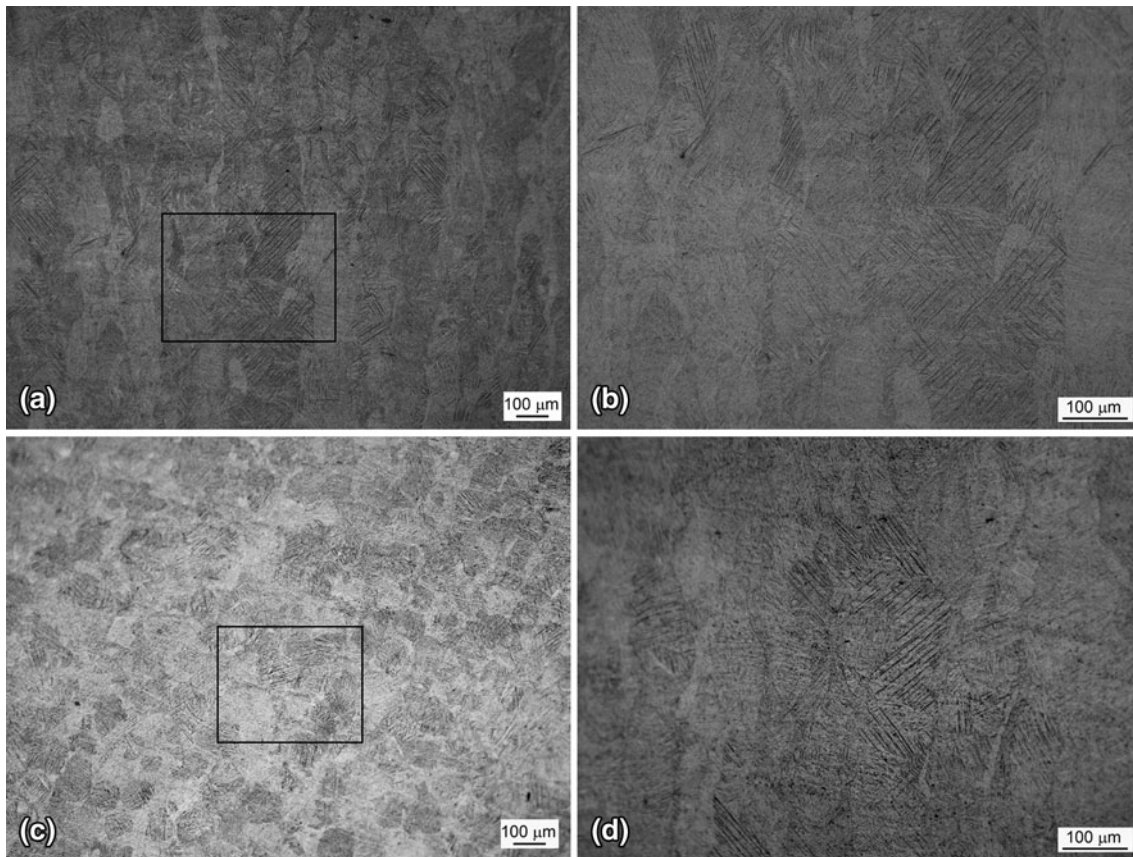


**Fig. 4** Optical micrographs of SLM-produced Ti64 samples. (a) Longitudinal cross-section showing columnar grains. (b) High magnification longitudinal cross-section image showing fine  $\alpha$  martensitic laths (from the boxed region in 'a'). (c) Transverse cross-section showing bundles of columnar grains. (d) High magnification transverse cross-section image showing fine  $\alpha$  martensitic laths in a columnar grain (from the boxed region in 'c')

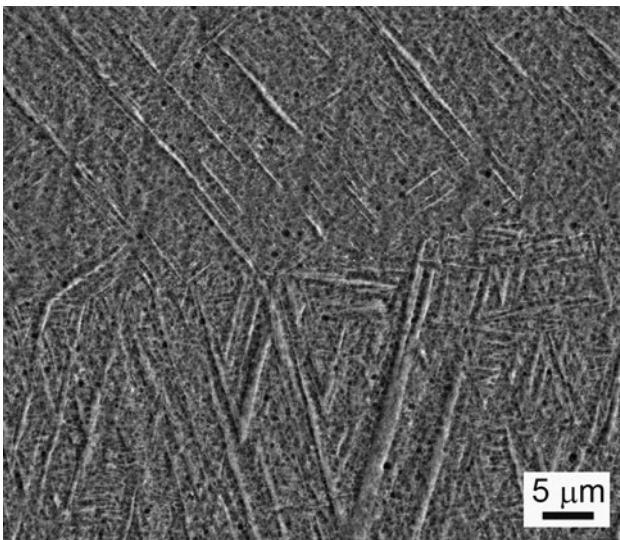


**Fig. 5** SEM-SE image of SLM-produced Ti64 sample

phase composition. Tensile tests at room temperature were performed for samples built in both vertical and horizontal orientations using an Instron 50 kN tensile testing machine. Rockwell hardness testing was carried out using a Wilson Rockwell Hardness 3JR tester. High cycle fatigue tests at room temperature were performed on a 10 kN Instron Electropulse

10000 fatigue testing machine. Fatigue tests were performed at a stress ratio of  $R = 0.1$  and a sinusoidal frequency of 50 Hz. Fatigue tests were stopped when specimens broke or the fatigue cycles reached  $10^7$  cycles.

### 3. Results and Discussions

#### 3.1 Surface Characteristics

The external surfaces of the parts fabricated by SLM and EBM processes have different surface roughness because of the difference in scan speed, powder particle size, and layer thickness. Figure 2(a) and (b) shows as-built tensile samples produced by SLM and EBM, respectively. From the external appearance it is clear that there is a difference in the surface condition. Figure 2 shows magnified SEM images of the external surfaces of solid cylindrical specimens fabricated by SLM and EBM. The surfaces of parts fabricated by SLM are relatively smooth when compared to EBM fabricated parts. Figure 3(a) and (b) shows the external surfaces of vertical and horizontal SLM samples, respectively. The surfaces of vertically built samples are characterized by a wavy appearance without any discontinuity. For horizontally built cylindrical samples the curved surfaces are formed by consecutive steps. Figure 3(c) and (d) shows the external surface of EBM-produced samples in vertical and horizontal orientations,

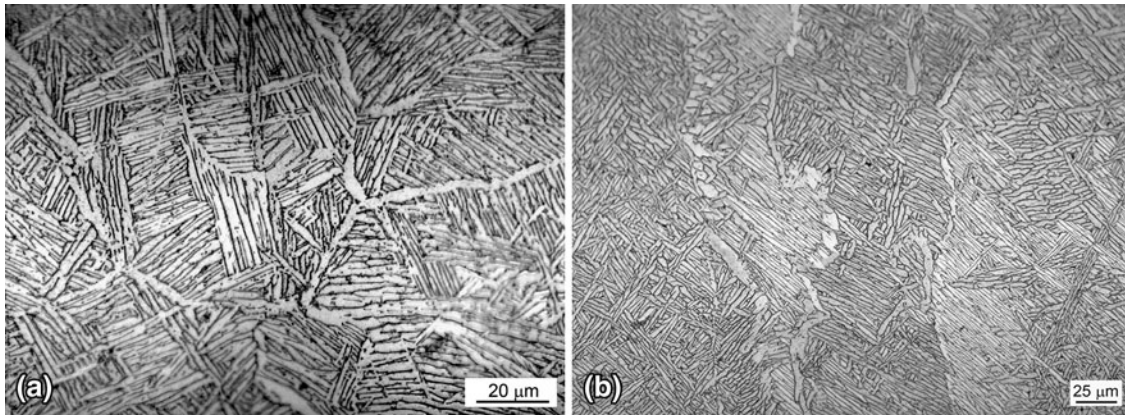


**Fig. 6** Optical micrograph of EBM-produced Ti64 samples. (a) Transverse cross-section. (b) Longitudinal cross-section

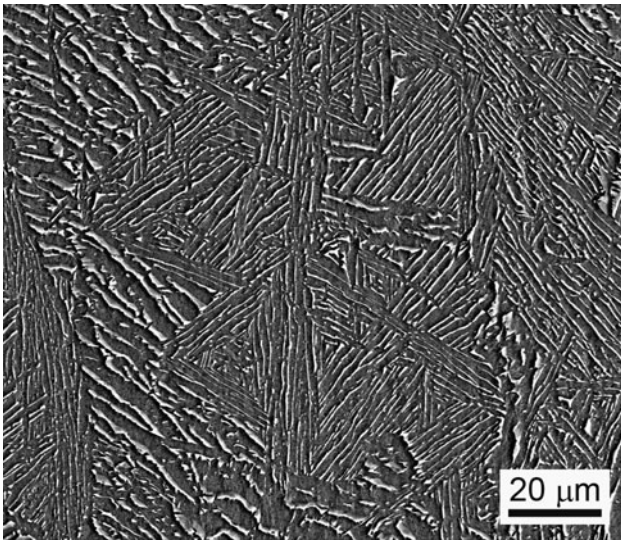


**Fig. 7** SEM-SE image showing Widmanstatten structure in EBM-produced Ti64 sample

respectively. Partly melted powders sticking to the surface and gaps showing distinct layers are visible at the external surface of vertically built samples. Similar to SLM samples, the horizontally built EBM sample surfaces also showed overlapping layers forming steps on the curved external surface.

The smooth surfaces for SLM fabricated parts are present due to the thinner layers, slower scan speeds, and finer powder particle sizes. The scan speed in EBM is an order of magnitude higher when compared to the scan speed in SLM. This makes the EBM process faster at the expense of poor surface finish. Formation of relatively thicker layers (70  $\mu\text{m}$  as compared to 30  $\mu\text{m}$  in SLM process) in the EBM process cause a more pronounced “stairstep effect” which results in a greater surface roughness. Surface conditions can have a significant effect on mechanical properties, particularly for fatigue. For many applications the parts must be subjected to machining to obtain a desired surface finish.

### 3.2 Microstructure

Microstructural evolution is primarily a function of cooling rate. The materials processed in SLM and EBM undergo very

high cooling rates. Figure 4 shows the optical microstructure of SLM processed Ti64. SLM processing of Ti64 resulted in a complete martensitic ( $\alpha'$ ) microstructure as expected (Ref 7). Martensitic laths originated from the prior  $\beta$  grain boundaries and fill the columnar grains. The morphology of lath martensite can be observed from the SEM-SE image shown in Fig. 5. The martensitic lath width is about 1-2  $\mu\text{m}$  and the length is close to the width of the columnar grains.

The optical micrographs of EBM-produced Ti64 given in Fig. 6 show a completely different microstructure. The microstructure is mainly composed of an  $\alpha$  phase and a small amount of  $\beta$  within the prior  $\beta$  columnar grains oriented along the build direction. The  $\alpha$  phase possesses a lamellar morphology with  $\beta$  surrounding the  $\alpha$  lamellae boundary. The  $\alpha$  lamellae are arranged in a Widmanstatten/basket weave structure with different sizes and orientations, and forms alpha platelet colonies within the columnar grains as can be seen in Fig. 7. This means that the SLM and EBM processes produce different microstructures at least for Ti64. However, in both cases prior  $\beta$  columnar grain boundaries are clearly visible. This implies that the primary mode of solidification still remains  $\beta$ , which is characteristic of Ti64 alloys irrespective of the process. Therefore the difference in microstructure is because of the differences in cooling rate when the  $\beta$  transforms to  $\alpha$  as it cools through the transus temperature. Since the SLM process has cooling rates on the order of  $10^6$  K/s, this results in the transformation of  $\alpha$  to  $\alpha'$ .

For EBM the build chamber is maintained at a temperature of 650-700  $^{\circ}\text{C}$  which is well above the  $M_s$  temperature for Ti64. Therefore, even though the cooling rates are higher at elevated temperatures, the material cools down to an isothermal temperature of 650-700  $^{\circ}\text{C}$ . This does not allow the transformation of  $\alpha$  to  $\alpha'$ . After completion of the build, the slow cooling rates from 700  $^{\circ}\text{C}$  to room temperature within the build chamber result in the formation of  $\alpha$  platelets. This means that there would be a corresponding difference in mechanical properties between SLM-processed and EBM-processed samples.

The microstructures of SLM- and EBM-produced Ti64 also differ from the microstructure of conventional wrought materials as shown in Fig. 8. The wrought Ti64 microstructure is composed of both  $\alpha$  and  $\beta$  grains oriented in the rolling direction. The suitability of the microstructure obtained from SLM and EBM processes for different applications are still a matter of debate. Since Ti64 and many other alloys respond

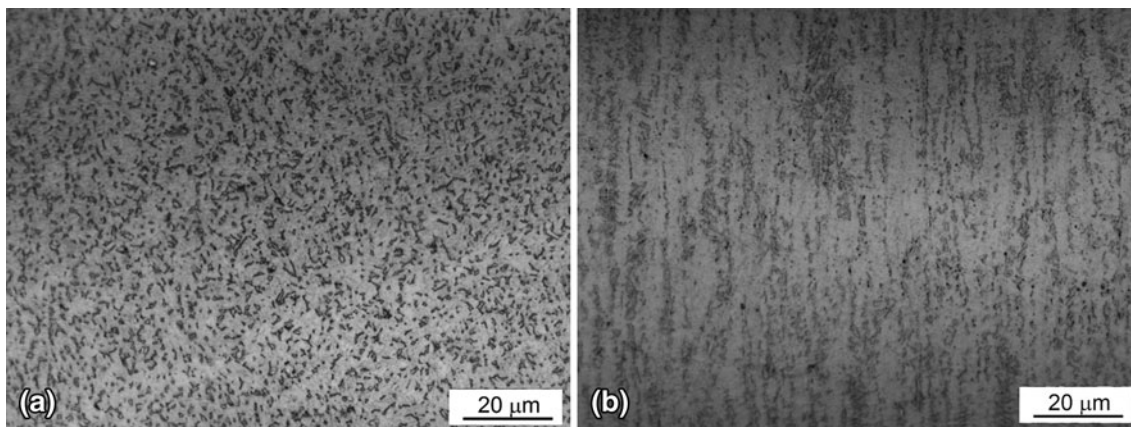


**Fig. 8** Optical micrograph of wrought Ti64 (annealed and rolled). (a) Transverse cross-section. (b) Longitudinal cross-section

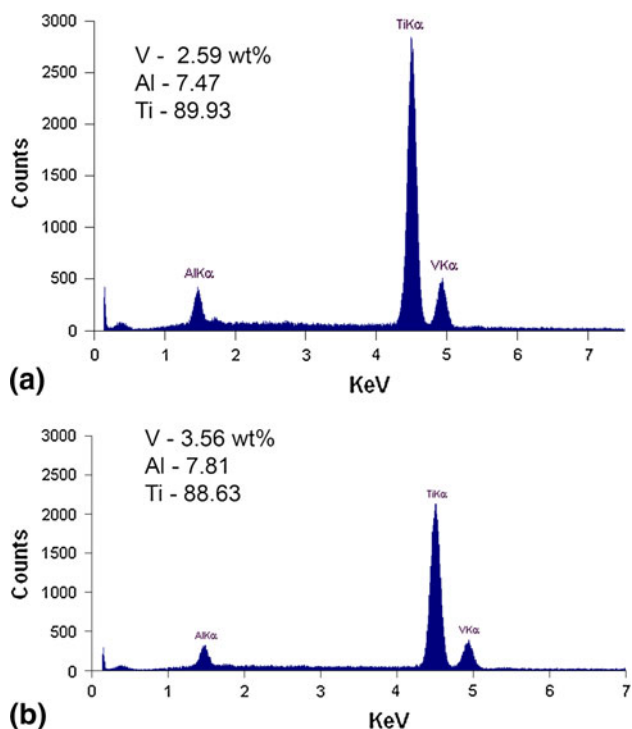


**Fig. 9** EDS spectrum and the composition in wt% of Ti64 samples produced by (a) SLM and (b) EBM

well to different heat treatments, selecting an appropriate post-heat treatment method can likely give the desired properties (Ref 14).

### 3.3 Composition and Phase Analysis

The chemical composition of SLM- and EBM-produced samples was compared using SEM-EDS. Though SEM-EDS is a semi quantitative method which lacks accuracy for obtaining the exact chemical composition, it is quite good for comparative purpose. Figure 9(a) and (b) shows the EDS spectrum and the composition in wt.% for SLM Ti64 and EBM Ti64, respectively. No significant difference is observed in the chemical composition, indicating that the formation of martensite in SLM Ti64 is not influenced by a variation in alloying element composition.

Figure 10(a) and (b) shows the XRD spectrum of SLM-processed Ti64 and EBM-processed Ti64, respectively. Analysis of XRD patterns from the SLM- and EBM-processed Ti64 show similar diffraction patterns. All the peaks can be identified as  $\alpha/\alpha'$ . As  $\alpha$  and  $\alpha'$  have the same crystal structure, hcp, it is difficult to differentiate the peaks though they are two different phases. However, the peak intensities in SLM-processed Ti64 are slightly lower compared to the spectra of EBM-processed Ti64. This is because of the finer structure in SLM-processed Ti64.

### 3.4 Tensile Properties

Tensile results of EBM- and SLM-produced Ti64 samples are summarized in Table 1. Corresponding stress-strain curves are shown in Fig. 11. The results are the mean values based on five duplicate tests. The yield strength, ultimate tensile strength, and percentage strain were obtained as direct output from the tensile testing machine. The percentage strain-to-failure was measured using a clip-on extensometer that was attached to the gage section of the test specimen. Substantial difference in tensile properties can be seen between the EBM-produced Ti64 and the SLM-produced Ti64 samples. However, the tensile strength values are comparable with or even better than the standard Ti64 material data given in the ASM Handbook (Ref 15). The tensile results are due to the differences observed in the microstructures. The higher tensile strength observed in SLM-produced Ti64 can be attributed to the martensitic microstructure as compared to the  $\alpha$  lamellar structure in EBM-produced Ti64 samples. Vilaro et al. (Ref 16) and Facchini et al. (Ref 17) also reported higher yield and ultimate strengths for as-fabricated SLM Ti64 specimens. Though the yield strength and tensile strength of EBM-produced Ti64 samples are low when compared to the SLM-produced Ti64 samples, the strain at break is higher indicating good ductility. The tensile strength values reported by Facchini et al. (Ref 13), Al-Bermani (Ref 12), and Chahine et al. (Ref 18) for EBM-produced Ti64 samples are similar to the results obtained in the current study. However, the tensile strength values reported by Murr et al. are slightly higher than the values reported in this study (Ref 6). The ultimate tensile strengths for both SLM- and EBM-produced Ti64 samples are only marginally higher than their yield strengths indicating the work hardening rate beyond the yield point is low.

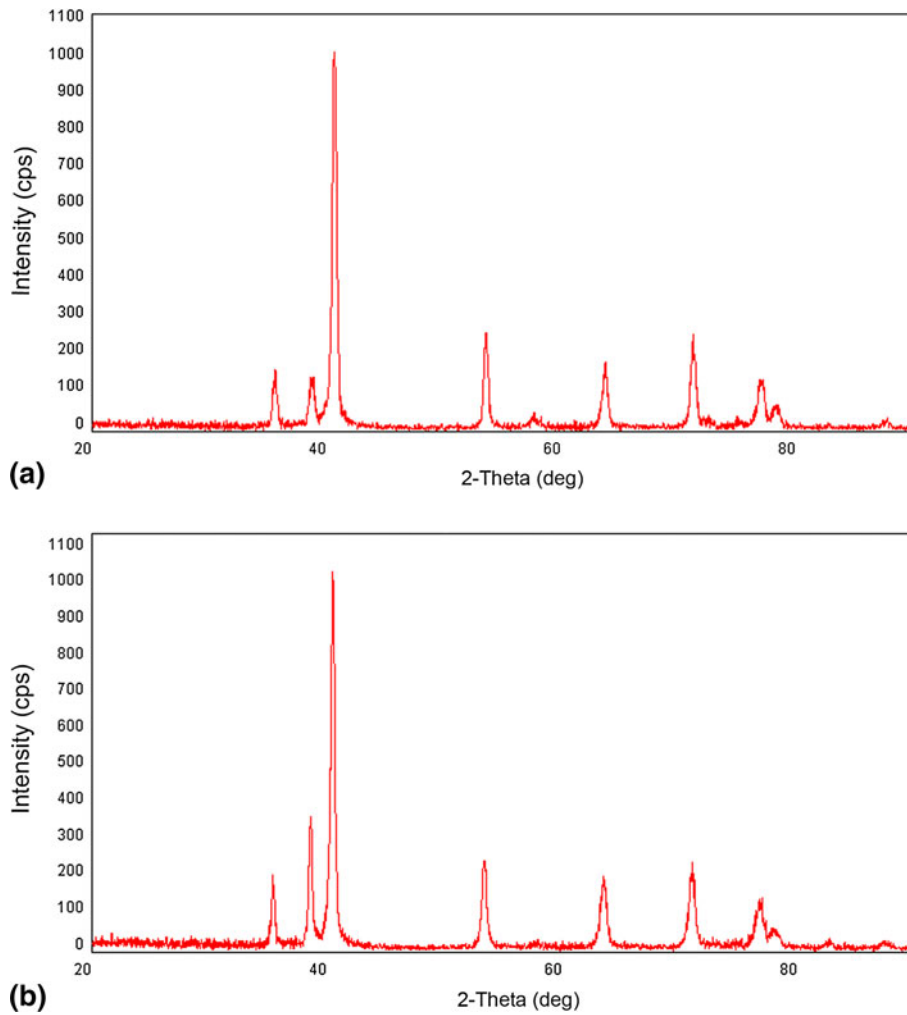


**Fig. 10** XRD spectrum of Ti64 samples produced by (a) SLM and (b) EBM

**Table 1** Tensile results for SLM-produced and EBM-produced Ti64 alloy samples

	Stress at yield (Offset 0.2%), MPa	Ultimate tensile stress, MPa	Strain at break, %
EBM (vertically built and Machined)	869 (SD: 7.2)	928 (SD: 9.8)	9.9 (SD: 1.7)
SLM (vertically built and Machined)	1143 (SD: 30)	1219 (SD: 20)	4.89 (SD: 0.6)
% Increase	31	31	-50
EBM (horizontally built and Machined)	899 (SD: 4.7)	978 (SD: 3.2)	9.5 (SD: 1.2)
SLM (horizontally built and Machined)	1195 (SD: 19)	1269 (SD: 9)	5 (SD: 0.5)
% increase	33	30	-47
ASM Handbook (Ref 15) (cast and annealed)	885	930	

SD: standard deviation

The tensile test results are in conformation with the bulk hardness tests. The Rockwell hardness test resulted in higher hardness for SLM-processed Ti64 (HRC: 41) compared to the hardness of EBM-processed Ti64 (HRC: 33).

Martensitic microstructure in Ti64 results in high strength and low ductility. Because of the low ductility, the SLM Ti64 samples failed at lower strain values. Ductility of SLM-produced Ti64 samples can be improved by proper post-heat treatment which decomposes the harder martensitic phase to

softer  $\alpha$  phase (Ref 14). The tensile properties of EBM-produced Ti64 sample are greatly influenced by the alpha lath width and alpha colony size in the microstructure. Coarsened  $\alpha$  phase and larger  $\alpha$  colony size results in the reduction of tensile strength (Ref 12). In EBM processes the morphology of the  $\alpha$  phase is primarily determined by the temperature maintained in the build chamber. A slight increase in build chamber temperature can cause coarsening of the  $\alpha$  phase and thereby causes a reduction in tensile strength. Another factor which

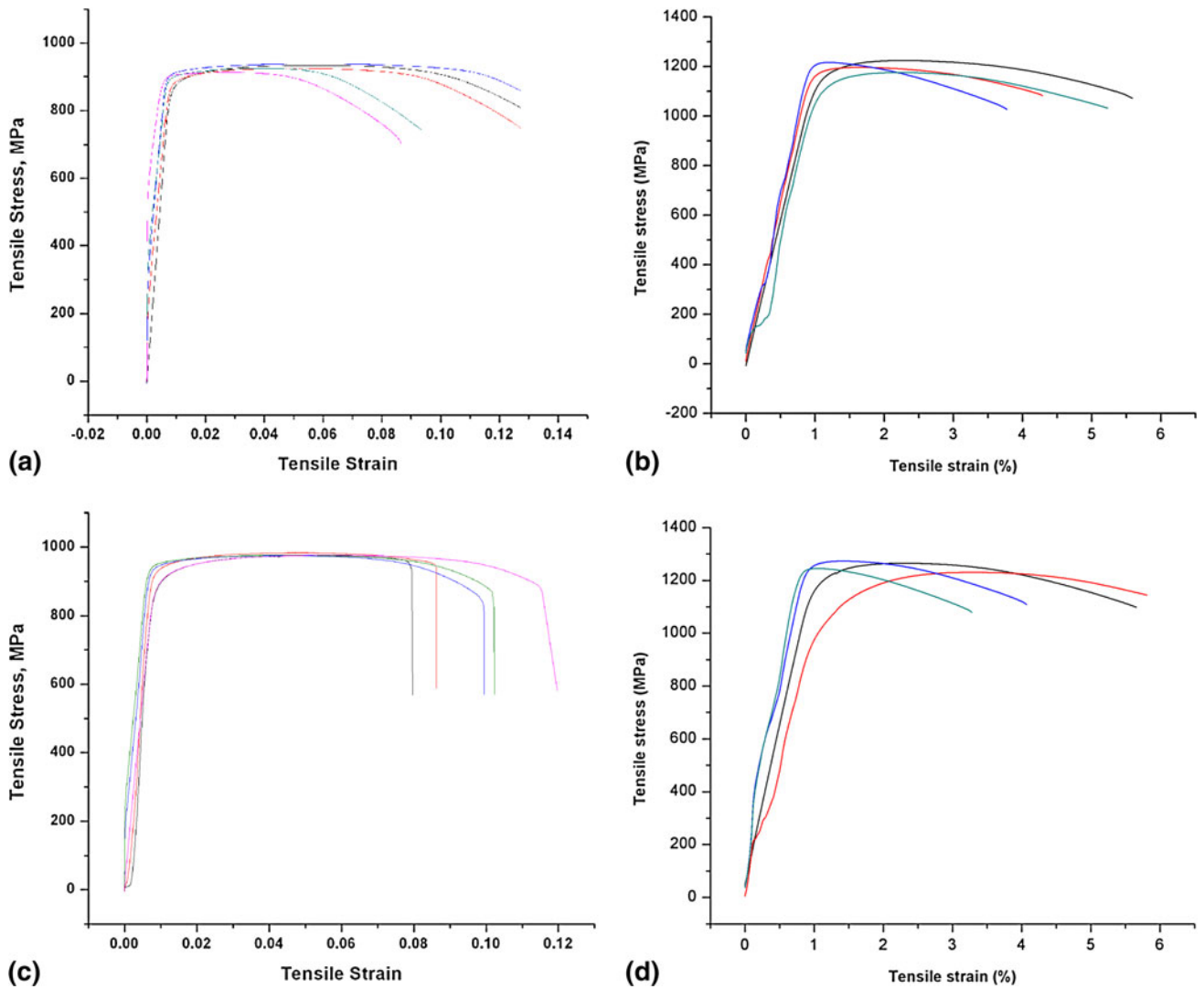


Fig. 11 Stress-Strain plots of Ti64 samples (a) EBM specimen built in vertical orientation, (b) SLM specimen built in vertical orientation, (c) EBM specimen built in horizontal orientation and (d) SLM specimen built in horizontal orientation

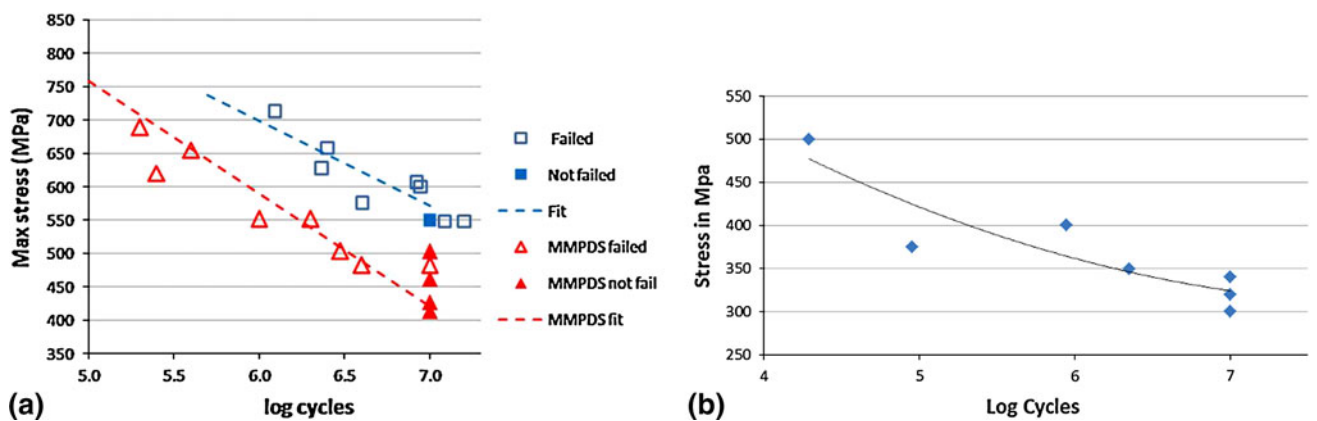
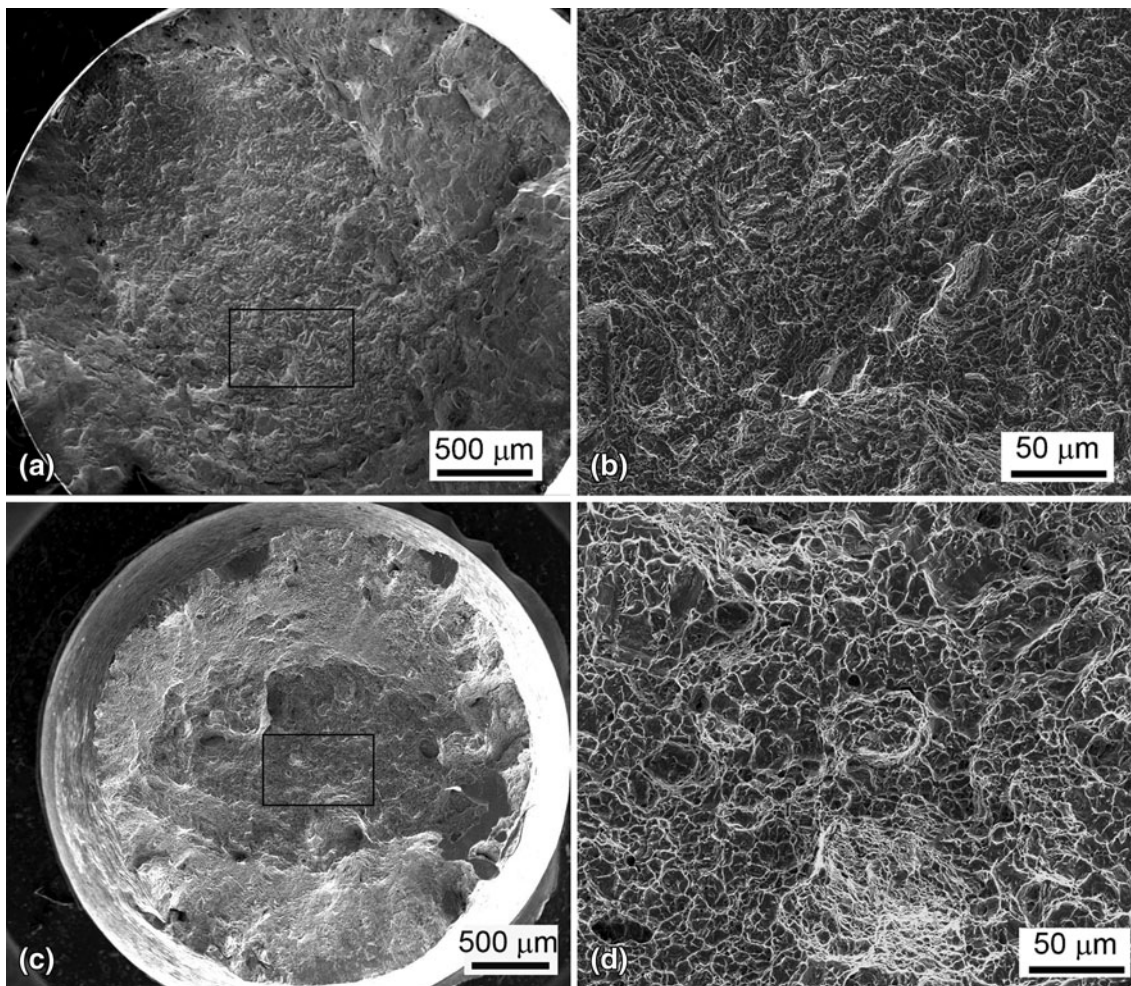


Fig. 12 S-N curve showing fatigue behavior of Ti64 samples (a) SLM and (b) EBM

affects the tensile properties is a chemical difference. This becomes a major concern when the Ti64 powder is recycled many times. Though there would not be any change in the

composition of major alloying elements like V and Al, over time the Ti64 powder picks up oxygen due to the high affinity of Ti for oxygen (Ref 12).





**Fig. 13** SEM-SE images of tensile fracture surfaces. (a) Overall view of SLM-produced Ti64 tensile fracture surface. (b) Enlarged view from the boxed region in “a.” (c) Overall view of EBM-produced Ti64 tensile fracture surface. (d) Enlarged view from the boxed region in “c”

### 3.5 Fatigue Properties

S-N curves illustrating the fatigue behavior of SLM-produced Ti64 and EBM-produced Ti64 are shown in Fig. 12. For SLM-produced Ti64 samples a fatigue limit of 550 MPa was observed (Fig. 12a). A comparison with MMPDS (Metallic Materials Properties Development and Standardization Handbook, Battelle Memorial Institute, Columbus, Ohio, April 2010) fatigue data shows better fatigue performance for Ti64 specimens built using SLM compared to Ti64 that is cast and annealed (430 MPa). However, the fatigue performance of EBM-produced Ti64 samples was inferior (Fig. 12b, fatigue limit: 340 MPa) as compared to the SLM-produced Ti64 and the MMPDS data. The better fatigue strength properties of SLM-produced Ti64 can be attributed to the martensitic phase. Martensite impedes dislocation motion and thus leads to a strengthening effect. Because of this strengthening effect, the total strain amplitude introduced during fatigue testing causes smaller plastic strain.

### 3.6 Fracture Behavior

**3.6.1 Tensile Fracture.** Representative fractographs of the tensile fracture surface of SLM- and EBM-produced Ti64 samples are shown in Fig. 13. SLM-produced Ti64 sample

fracture surfaces exhibited a mixed mode of brittle and ductile fracture (Fig. 13a, b) showing predominantly cleavage facets. Cleavage fracture is a low energy brittle fracture which propagates along low index crystallographic planes (Ref 19). This fracture is characterized by flat, cleavage facets. River markings separating the facets result from the propagation of the crack on a number of planes of different levels (Ref 20). The fracture surface of EBM-produced Ti64 sample is characterized by transgranular ductile dimple tearing resulting from the coalescence of microvoids (Fig. 13c, d). A healthy population of fine dimples at the tensile fracture surface indicates the extent of plastic deformation.

**3.6.2 Fatigue Fracture.** Figure 14 shows the fatigue fracture surfaces of SLM-produced Ti64 and EBM-produced Ti64. In SLM-produced Ti64 samples (Fig. 14a, b) the crack initiated from an internal defect and propagated radially outwards. Three distinct regions show crack initiation, steady crack growth, and overload regions typical for fatigue fracture. The crack propagation looks more tortuous as it propagated through multiple crystallographic planes. The fracture surface of EBM-produced Ti64 samples appear normal, with a characteristic fatigue fracture surface (Fig. 14c). The crack initiation site is characterized by microscopically smooth facets away from the surface as evident from Fig. 14(d). It can also be

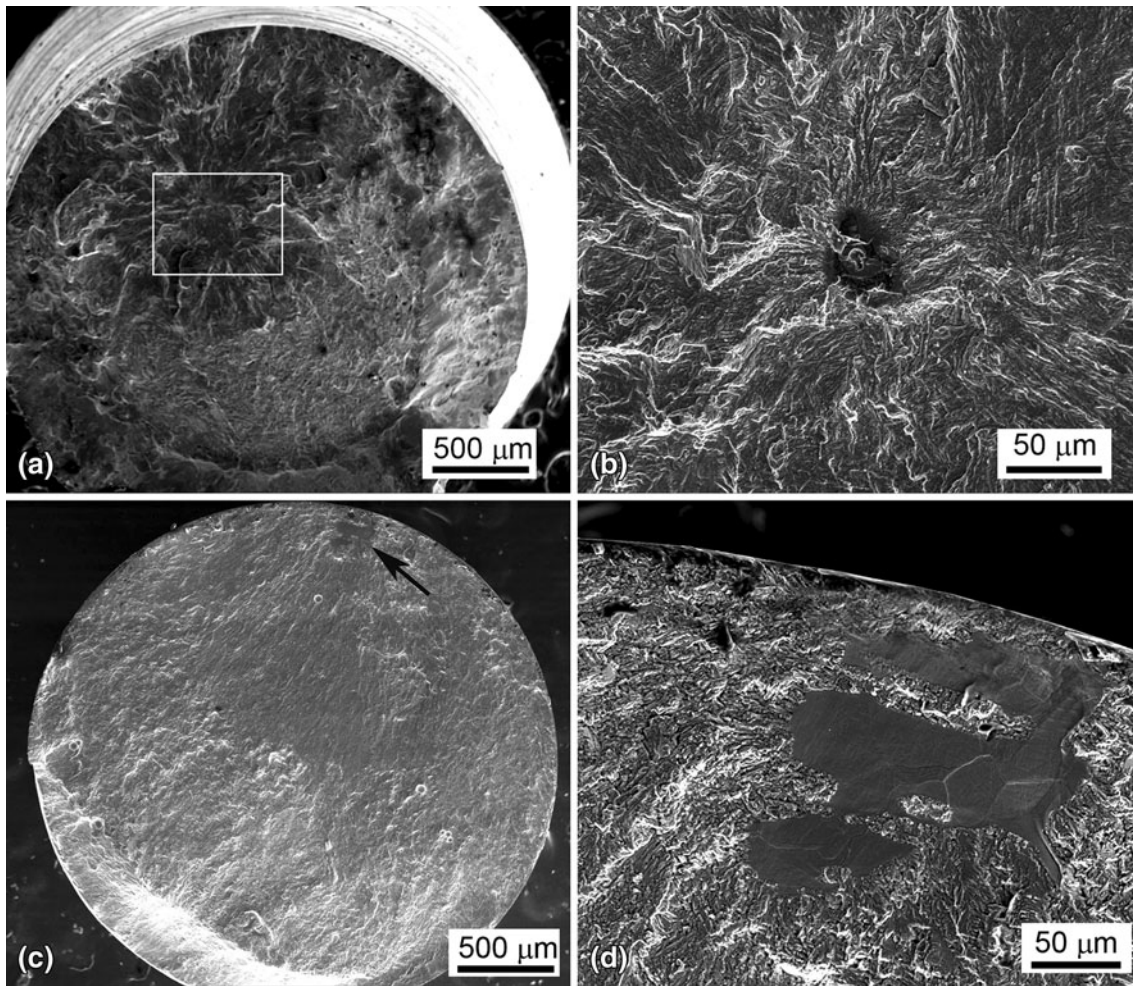


**Fig. 14** SEM-SE images of fatigue fracture surfaces. (a) Overall view of SLM-produced Ti64 fracture surface. (b) Enlarged view from the boxed region in “a.” (c) Overall view of EBM-produced Ti64 fracture surface. (d) Enlarged view from the arrow pointed region in “c”

noted that the crack initiation site has multiple facets which could possibly be due to crack initiation occurring at the  $\alpha$  colony boundaries and shear across neighboring  $\alpha$  colonies. This indicates that crack initiation is not caused by the classical slip-band intrusion/extrusion mechanism. Therefore, one common feature that can be seen between the fatigue fracture surfaces of SLM- and EBM-produced Ti64 samples is that the crack initiation occurred from the interior or the sub surface and not from the external surface. In general, for metallic materials fatigue crack initiation occurs at the surface if the sample is free from large internal defects. Previous studies show that this may not be true in the case of Ti64 with dual phase microstructures. In  $\alpha/\beta$  titanium alloys, cracks tend to initiate either at the surface or at the subsurface or at the impingement of slip bands within the alpha lamellae of a fully lamellar microstructure. They can also initiate at the boundaries separating the  $\alpha$  and  $\beta$  phase (Ref 21).

Fatigue behavior of Ti64 is greatly influenced by its microstructure. Depending on the process conditions the morphology and volume fraction of  $\alpha$  and  $\beta$  constituents in Ti64 changes. The microstructure of Ti64 can exist in forms such as bi-modal, equiaxed, lamellar  $\alpha$  and  $\beta$ , and martensitic  $\alpha'$  structures. All these microstructures can result in different fatigue properties. As observed earlier, Ti64 processed by SLM resulted in martensitic  $\alpha'$  and EBM resulted in lamellar  $\alpha$  with

smaller amount of  $\beta$ . Ivanova et al. observed that in the high cycle fatigue regime the preferred crack initiation sites are within the alpha grains in an equiaxed grain structure. The crack nucleates along the slip bands within the alpha grain and results in cleavage fracture (Ref 22). For a bimodal microstructure the crack initiates by the cracking of suitably oriented  $\alpha$  grains and subsequent growth along the planar slip bands within interconnected  $\alpha$  grains. Crack initiation occurs by cross-colony slip-band fracture for the lamellar microstructure (Ref 23). Oh et al. showed that fatigue crack initiation occurs mainly at the prior  $\beta$  grain boundary for an electron beam welded and then annealed Ti64 sample. They also observed that the large micropores present in the weld act as fatigue crack initiation sites. However, the micropores did not have any effect on crack propagation (Ref 24). In titanium alloys, an increase in oxygen content can also lead to the embrittlement of the alpha phase. Among the different characteristic microstructures exhibited by Ti64, lamellar structures are more prone to crack initiation as compared to equiaxed or bi-modal structures. But for crack propagation, lamellar structures offer greater resistance to crack growth than equiaxed structures. In high cycle fatigue, crack initiation forms the major part of the fatigue life. To increase the resistance to fatigue crack nucleation, the maximum dislocation slip length in the microstructure should be reduced. Generally, a fatigue crack nucleates due to

irreversible slip bands within the longest crystallographic planes available in the microstructure. Consequently, coarse lamellar microstructures with colonies of aligned  $\alpha$  and extended planar-slips running across these colonies often have less resistance to crack nucleation when compared to fine-grained equiaxed and acicular martensitic microstructures (Ref 23). Therefore, the inferior fatigue strength of EBM samples could be attributed to its lamellar microstructure rather than due to the presence of micropores or voids.

## 4. Summary

In this study an attempt was made to highlight the differences between SLM and EBM processes concerning Ti64. A clear difference in surface conditions, microstructure, tensile properties, and fatigue properties are evident. The primary difference between the processes boils down to the cooling rate. The same material processed using SLM and EBM can have different properties. Irrespective of the processes, what matters is the suitability of a final part for a specific application. Ti64 is considered for very wide range of applications from biomedical to aerospace. The property requirements for a part produced for biomedical applications may differ from a part produced for aerospace applications. As discussed earlier, processing of Ti64 with SLM and EBM results in microstructures containing  $\alpha'$ ,  $\alpha$ , and  $\beta$  phases. With respect to the volume fraction of these phases and their morphology the resulting properties will vary to a certain extent. For instance, the higher hardness possessed by  $\alpha'$  phases may be beneficial for certain applications and on the other hand it may be detrimental for some other applications. Therefore, selection of a particular process, whether SLM or EBM, primarily depends on the requirements for end-use. For that, one should have a proper understanding of the structure-property relationship of the material chosen.

## 5. Conclusions

This comparative study on SLM and EBM processes when using Ti64 as the build material has resulted in the following conclusions:

1. The surface finish of SLM-produced samples is better than EBM-processed samples. Relatively thick layers in EBM cause more pronounced “stairstep effects” and larger particle size powders adhering to the surface result in rougher surfaces.
2. The SLM-produced and EBM-produced samples resulted in two different microstructures for Ti64. SLM-produced Ti64 resulted in martensitic  $\alpha'$  microstructures and EBM-produced Ti64 resulted in an  $\alpha$  phase with  $\beta$  separating the  $\alpha$  lamellae.
3. SLM-produced Ti64 samples have higher tensile strength than EBM-produced samples. But EBM-produced samples have higher ductility. Higher tensile strength of SLM samples is attributed to the martensitic  $\alpha'$  microstructure and the higher ductility in EBM-produced samples is attributed to the lamellar  $\alpha$  phase.
4. The SLM-produced samples showed a fatigue limit of 550 MPa, whereas EBM-produced samples showed

a fatigue limit of 340 MPa. The inferior fatigue limit observed for EBM is because of the lamellar phase microstructure.

5. Selecting between SLM and EBM for fabrication of a specific Ti64 part depends on the application requirements as both result in mechanical properties suitable for many applications.

## Acknowledgments

The authors acknowledge the Office of Naval Research (ONR), USA for support through grant #'s N00014-09-1-0147, N00014-10-1-0800, and N00014-11-1-0689.

## References

1. F. Abe, K. Osakada, M. Shiomi, K. Uematsu, and M. Matsumoto, The Manufacturing of Hard Tools from Metallic Powders by Selective Laser Melting, *J. Mater. Process. Technol.*, 2001, **111**, p 210–213
2. S.M. Gaytan, L.E. Murr, E. Martinez, J.L. Martinez, B.I. Machado, D.A. Ramirez, F. Medina, S. Collins, and R.B. Wicker, Comparison of Microstructures and Mechanical Properties for Solid and Mesh Cobalt-Base Alloy Prototypes Fabricated by Electron Beam Melting, *Metall. Mater. Trans. A*, 2010, **41A**, p 3216–3227
3. E. Brinksmeier, G. Levy, D. Meyer, and A.B. Spierings, Surface Integrity of Selective-Laser-Melted Components, *CIRP Ann. Manuf. Technol.*, 2010, **59**(1), p 601–606
4. J.P. Kruth, G. Levy, F. Klocke, and T.H.C. Childs, Consolidation Phenomena in Laser and Powder-Bed Based Layered Manufacturing, *CIRP Ann. Manuf. Technol.*, 2007, **56**, p 730–759
5. M.F. Zah and S. Lutzmann, Modelling and Simulation of Electron Beam Melting, *Prod. Eng. Res. Dev.*, 2010, **4**, p 15–23
6. L.E. Murr, E.V. Esquivel, S.A. Quinones, S.M. Gaytan, M.I. Lopez, E.Y. Martinez, F. Medina, D.H. Hernandez, E. Martinez, J.L. Martinez, S.W. Stafford, D.K. Brown, T. Hoppe, W. Meyers, U. Lindhe, and R.B. Wicker, Microstructures and Mechanical Properties of Electron Beam-Rapid Manufactured Ti-6Al-4V Biomedical Prototypes Compared to Wrought Ti-6Al-4V, *Mater. Charact.*, 2009, **60**, p 96–109
7. L. Thijss, F. Verhaeghe, T. Craeghs, J.V. Humbeeck, and J.P. Kruth, A Study of the Microstructural Evolution During Selective Laser Melting of Ti-6Al-4V, *Acta Mater.*, 2010, **58**, p 3303–3312
8. B. Song, S. Dong, B. Zhang, H. Liao, and C. Coddet, Effects of Processing Parameters on Microstructure and Mechanical Property of Selective Laser Melted Ti6Al4V, *Mater. Des.*, 2012, **35**, p 120–125
9. I. Yadroitsev, P. Bertrand, and I. Smurov, Parametric Analysis of the Laser Melting Process, *Appl. Surf. Sci.*, 2007, **253**(19), p 8064–8069
10. R. Morgan, C.J. Sutcliffe, and W. O'Neill, Density Analysis of Direct Metal Laser Remelted 316L Stainless Steel Cubic Primitives, *J. Mater. Sci.*, 2004, **39**(4), p 1195–1205
11. E. Yasa, J. Deckers, and J.P. Kruth, The Investigation of the Influence of Laser Re-Melting on Density, Surface Quality and Microstructure of Selective Laser Melting Parts, *Rapid Prototyp. J.*, 2011, **17**(5), p 312–327
12. S.S. Al-Bermani, M.L. Blackmore, W. Zhang, and I. Todd, The Origin of Microstructural Diversity, Texture, and Mechanical Properties in Electron Beam Melted Ti-6Al-4V, *Metall. Mater. Trans. A*, 2010, **41A**, p 3422–3432
13. L. Facchini, E. Magalini, P. Robotti, and A. Molinari, Microstructure and Mechanical Properties of Ti-6Al-4V Produced by Electron Beam Melting of Pre-Alloyed Powders, *Rapid Prototyp. J.*, 2009, **15**(3), p 171–178
14. B. Vrancken, L. Thijss, J.P. Kruth, and J.V. Humbeeck, Heat Treatment of Ti6Al4V Produced by Selective Laser Melting—Microstructure and Mechanical Properties, *J. Alloy Compd.*, 2012, **541**, p 177–185
15. ASM Handbook, Vol. 1, ASM International, Materials Park, OH, 1993, p 2071

16. T. Vilaro, C. Colin, and J.D. Bartout, As-Fabricated and Heat Treated Microstructures of the Ti-6Al-4V Alloy Processed by Selective Laser Melting, *Metall. Mater. Trans. A.*, 2011, **42**, p 3190
17. L. Facchini, E. Magalini, P. Robotti, A. Molinari, S. Hogess, and K. Wissenbach, Ductility of Ti-6Al-4V Alloy Produced by Selective Laser Melting of Pre-Alloyed Powders, *Rapid Prototyp. J.*, 2010, **16**(6), p 450–459
18. G. Chahine, M. Koike, T. Okabe, P. Smith, and R. Kovacevic, The Design and Production of Ti-6Al-4V ELI, Customized Dental Implants, *JOM*, 2008, **60**(11), p 50–55
19. G.E. Dieter, *Mechanical Metallurgy*, McGraw Hill, New York, 1986
20. M. Erdogan and S. Tekeli, The Effect of Martensitic Particle Size on Tensile Fracture of Surface-Carburized AISI, 8620 Steel with Dual Phase Core Microstructure, *Mater. Des.*, 2002, **23**, p 597–604
21. T.S. Srivatsana, M. Kuruvilla, and L. Park, A Study at Understanding the Mechanisms Governing the High Cycle Fatigue and Final Fracture Behavior of the Titanium Alloy: Ti-4Al-2.5V, *Mater. Sci. Eng. A.*, 2010, **527**, p 435–448
22. S.G. Ivanova, R.R. Biederman, and R.D. Sisson, Jr., Investigation of Fatigue Crack Initiation in Ti-6Al-4V During Tensile-Tensile Fatigue, *J. Mater. Eng. Perform.*, 2002, **11**(2), p 226–231
23. R.K. Nalla, B.L. Boyce, J.P. Campbell, J.O. Peters, and R.O. Ritchie, Influence of Microstructure on High-Cycle Fatigue of Ti-6Al-4V: Bimodal vs. Lamellar Structures, *Metall. Mater. Trans. A.*, 2002, **33A**, p 899–918
24. J. Oh, N.J. Kim, S. Lee, and W. Lee, Correlation of Fatigue Properties and Microstructure in Investment Cast Ti-6Al-4V, *Mater. Sci. Eng. A.*, 2003, **340**, p 232–242